

Novel Operation Mode of the Modular Multilevel Matrix Converter based on a Dimensioning Algorithm

Rebecca Dierks, and Axel Mertens

Leibniz University Hannover

Institute for Drive Systems and Power Electronics

Hannover, Germany

Email: rebecca.dierks@ial.uni-hannover.de

URL: <http://www.ial.uni-hannover.de>

Acknowledgments

This research was funded by the German Research Foundation (DFG) – Project 254417319.

Keywords

«Modular Matrix Converter», «AC-to-AC Converter», «Converter Control»

Abstract

The focus of the proposed operation mode of the modular multilevel matrix converter is to find the optimal trade-off between branch energy variation and branch currents. For this purpose, a weighting function is used to calculate the optimal circulating current parameters. This novel approach is compared to existing operation modes and validated on a low-voltage test bench.

Introduction

The modular multilevel matrix converter (M3C) shown in Fig. 1 (a) can directly convert a three-phase AC to another three-phase AC system without a DC voltage link. This type of converter with a modular branch design was first introduced by Glinka *et al.* [1] for a single phase. In later publications, this technology was also developed for two three-phase systems. Compared to conventional matrix converters, higher voltage classes can be achieved by the modular structure and output voltages with lower harmonics can be obtained due to smaller voltage steps.

A typical application of the M3C is the connection of a three-phase medium-voltage drive to the grid [2]. Furthermore, recent publications present the approach of connecting, for example, offshore wind farms via Low-Frequency-HVAC transmission (LF-HVAC transmission) [3]. In this case, the M3C is used as an onshore converter and thus large offshore converter platforms like those involved in HVDC transmission can be eliminated. In both the drive application and LF-HVAC transmission application, the M3C control must ensure that the system is also functional at low frequencies.

Similar to the DC-AC modular multilevel converters, a cascaded control structure with an outer branch energy control and an inner current control can be used [4] [5]. This has the advantage that the energies and currents with significantly different control time constants can be controlled decoupled from each other. So-called circulating currents can be used as degrees of freedom when controlling the branch energies, as these only circulate inside the M3C and do not influence the external variables. Beside the circulating current components that are responsible for controlling the M3C, which occur only in the transient state, additional circulating currents which exist also in the steady state can further be injected. In a simple operation (Normal Mode) of the M3C without steady-state circulating currents, high branch energy variations occur when one connected system is operated with frequencies close to zero or when both systems have the same frequency. High branch energy variation leads to a high installed module

capacitance. For this reason, several operation modes have been introduced in the literature to reduce the branch energies. The operation modes of Korn *et. al* [6] introducing the Instantaneous Power Mode (IPM) and Kawamura *et. al* [7] introducing the mode Control III (Ctr3) deal with the injection of additional steady-state circulating currents to ensure the operation of the M3C even when one connected system is running at a low frequency. In addition, there are also several operation modes that deal with the situation where both connected systems have the same frequency and an additional injection of the star-point voltage can also be utilised as a degree of freedom [8] [9].

However, major disadvantages of these operation modes are that higher branch current losses occur due to the injection of additional circulating currents, and the operation modes do not consider a trade-off between branch energy variation and the resulting losses. This means that with a fixed module capacitor size, the branch energy variation often does not have to be reduced so drastically at lower frequencies and consequently not so high circulating currents have to be injected. For example in the publication of Engel et al. [10], the topology of the conventional Modular Multilevel Converter (M2C) is used to show how a trade-off between installed module capacitance and branch losses can be achieved when using a cost function containing branch energy variation and branch current at different modulation indices. In addition, as discussed in [11], the choice of the circulating current amplitudes should be made depending on the system frequencies. For example, the amplitudes of the circulating currents should be chosen relatively large if one of the connected systems operates at low frequencies in order to compensate the high branch energy variations. For increasing system frequencies, smaller circulating current amplitudes should be selected.

For this reason, the following operation mode is proposed, which is based on an analytical model determining the optimal weighting between installed module capacitances and occurring branch losses. When solving the optimisation problem, the optimal amplitudes of the circulating currents are calculated, which are dependent on the system frequencies. The new approach is derived with a generalised three-phase model with variable frequencies, so that the operation mode is suitable for both machine and LF-HVAC grid applications. Furthermore, the novel operation mode is validated on a low-voltage test bench.

Model Description of the Modular Multilevel Matrix Converter

This section gives a brief overview of the control structures used and the operation modes considered, which are derived from an analytical model.

Control Structure of the Modular Multilevel Matrix Converter

The M3C is controlled by the cascaded control system of Fig. 2, which is based on the approach of reference [4]. The branch energy control represents the outer control loop and is responsible for distributing the energy stored in the capacitors evenly between the branches. The current control setpoints resulting from the branch energy control are controlled in the inner current control loop. In the current control, the state space vector with

$$\mathbf{x}' = [\mathbf{x} \quad v_{st}]^T = [i_{X\alpha} \quad i_{X\beta} \quad i_{Y\alpha} \quad i_{Y\beta} \quad i_{cir1} \quad i_{cir2} \quad i_{cir3} \quad i_{cir4} \quad v_{st}]^T \quad (1)$$

represents the variables that need to be controlled. The vector \mathbf{x} contains the system currents in alpha-beta coordinates of the system X with $i_{X\alpha}, i_{X\beta}$ and of the system Y with $i_{Y\alpha}, i_{Y\beta}$ and the four circulating currents $\mathbf{i}_{cir} = [i_{cir1} \quad i_{cir2} \quad i_{cir3} \quad i_{cir4}]^T$. In addition, the state space vector \mathbf{x}' is extended by the star-point voltage v_{st} , which also represents a degree of freedom in the control of the M3C. To implement different operation modes, additional circulating currents $\mathbf{i}_{cir,add}$ in

$$\mathbf{x}'_{add} = [0 \quad 0 \quad 0 \quad 0 \quad i_{cir1,add} \quad i_{cir2,add} \quad i_{cir3,add} \quad i_{cir4,add} \quad 0]^T \quad (2)$$

are injected as offset circulating currents. The setpoints for the branch voltages $\mathbf{u}^* = \mathbf{v}_b^*$ with v_{bij}^* are calculated with the state space representation, as shown in Fig. 2. Index $i \in \{1, 2, 3\}$ stands for the phase of system X and $j \in \{1, 2, 3\}$ for the phase of system Y. A more detailed description of the control structure can be found in [4].

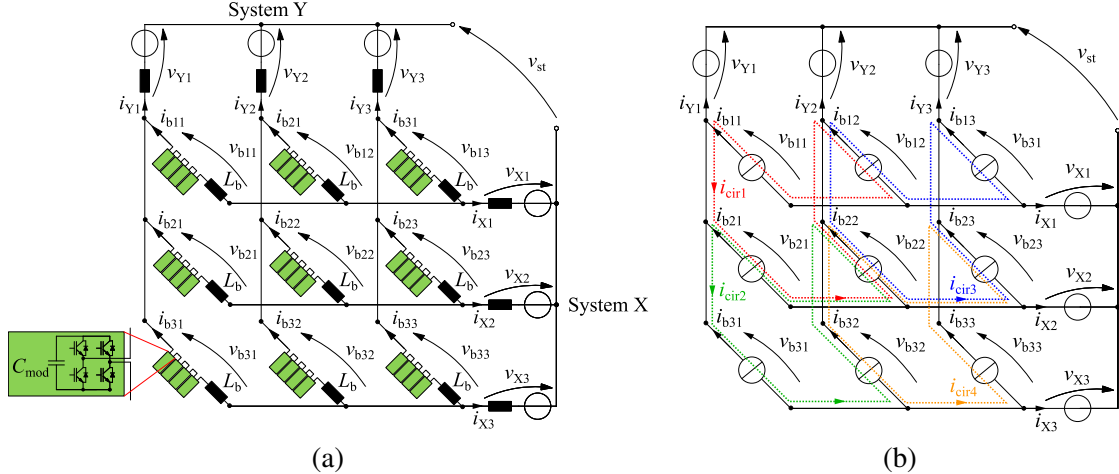


Fig. 1: Modular multilevel matrix converter: (a) configuration (b) simplified model

Analytical Derivation of the Operation Modes

For the derivation of the operation modes, an analytical model with a simplified equivalent circuit diagram (ECD) of the M3C from Fig. 1 (b) is considered. It is assumed that the current control reacts infinitely fast and thus the branch voltage source can be replaced by a branch current source and the branch inductance and branch losses can be neglected. Furthermore, system X and system Y are each represented by three voltage sources, which describe the voltages measured at the outputs of the converter. By using the node equations of the simplified ECD, the branch currents can be transformed with the matrix \mathbf{T}_{ib} into

$$\mathbf{i}_b = [i_{b11} \quad i_{b12} \quad i_{b13} \quad i_{b21} \quad i_{b22} \quad i_{b23} \quad i_{b31} \quad i_{b32} \quad i_{b33}]^T = \mathbf{T}_{ib} \cdot [\mathbf{i}_x \quad \mathbf{i}_y \quad \mathbf{i}_{cir}]^T . \quad (3)$$

The used convention of the circulating currents \mathbf{i}_{cir} can be taken from Fig. 1 (b). In addition, the three-phase system currents $\mathbf{i}_X = [i_{X1} \quad i_{X2} \quad i_{X3}]^T$ and $\mathbf{i}_Y = [i_{Y1} \quad i_{Y2} \quad i_{Y3}]^T$ are simplified as symmetrical currents

$$\mathbf{i}_X = \sqrt{2} \cdot I_X \cdot \begin{bmatrix} \cos(\theta_X - \phi_X) \\ \cos(\theta_X - \frac{2\pi}{3} - \phi_X) \\ \cos(\theta_X - \frac{4\pi}{3} - \phi_X) \end{bmatrix} \quad \text{and} \quad \mathbf{i}_Y = \sqrt{2} \cdot I_Y \cdot \begin{bmatrix} \cos(\theta_Y - \phi_Y + \psi) \\ \cos(\theta_Y - \frac{2\pi}{3} - \phi_Y + \psi) \\ \cos(\theta_Y - \frac{4\pi}{3} - \phi_Y + \psi) \end{bmatrix} \quad (4)$$

with the phase differences ϕ_X and ϕ_Y between voltage and current and with the rotation angles $\theta_X = \omega_X \cdot t$ and $\theta_Y = \omega_Y \cdot t$. Furthermore, the angle ψ indicates the phase shift between system X and system Y. Similar to the description of the currents, the branch voltage vector

$$\mathbf{v}_b = [v_{b11} \quad v_{b12} \quad v_{b13} \quad v_{b21} \quad v_{b22} \quad v_{b23} \quad v_{b31} \quad v_{b32} \quad v_{b33}]^T = \mathbf{T}_{vb} \cdot [\mathbf{v}_x \quad \mathbf{v}_y \quad v_{st}]^T \quad (5)$$

can be represented with the help of the mesh equation of the simplified ECD as a function of the system voltages $\mathbf{v}_X = [v_{X1} \quad v_{X2} \quad v_{X3}]^T$, $\mathbf{v}_Y = [v_{Y1} \quad v_{Y2} \quad v_{Y3}]^T$ and the star-point voltage v_{st} . The matrices \mathbf{T}_{ib} and \mathbf{T}_{vb} are shown in (6).

$$\mathbf{T}_{ib} = \frac{1}{9} \cdot \begin{bmatrix} 3 & 0 & 0 & -3 & 0 & 0 & 16 & 8 & 9 & 4 \\ 3 & 0 & 0 & 0 & -3 & 0 & -8 & -4 & 8 & 4 \\ 3 & 0 & 0 & 0 & 0 & -3 & -8 & -4 & -16 & -8 \\ 0 & 3 & 0 & -3 & 0 & 0 & -8 & 8 & -4 & 4 \\ 0 & 3 & 0 & 0 & -3 & 0 & 4 & -4 & -4 & 4 \\ 0 & 3 & 0 & 0 & 0 & -3 & 4 & -4 & 8 & -8 \\ 0 & 0 & 3 & -3 & 0 & 0 & -8 & -16 & -4 & -8 \\ 0 & 0 & 3 & 0 & -3 & 0 & 4 & 8 & -4 & -8 \\ 0 & 0 & 3 & 0 & 0 & -3 & 4 & 8 & 8 & 16 \end{bmatrix}, \quad \mathbf{T}_{vb} = \begin{bmatrix} 1 & 0 & 0 & -1 & 0 & 0 & 1 \\ 1 & 0 & 0 & 0 & -1 & 0 & 1 \\ 1 & 0 & 0 & 0 & 0 & -1 & 1 \\ 0 & 1 & 0 & -1 & 0 & 0 & 1 \\ 0 & 1 & 0 & 0 & 0 & -1 & 1 \\ 0 & 0 & 1 & -1 & 0 & 0 & 1 \\ 0 & 0 & 1 & 0 & -1 & 0 & 1 \\ 0 & 0 & 1 & 0 & 0 & -1 & 1 \end{bmatrix} \quad (6)$$

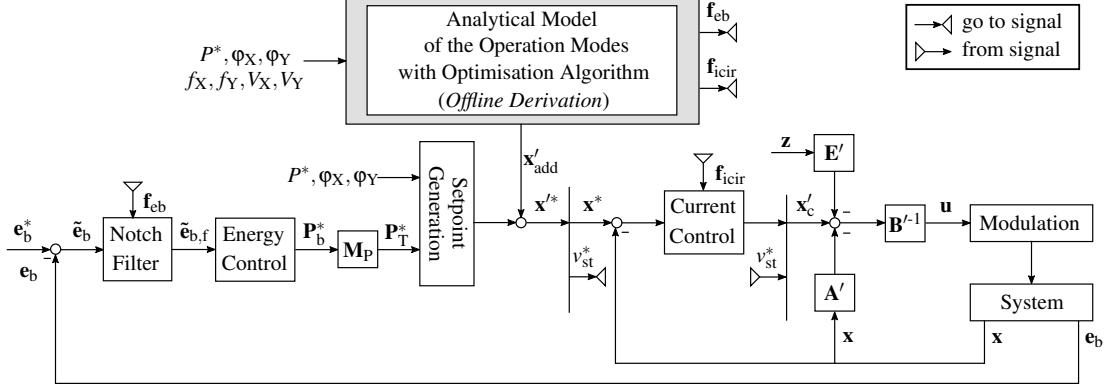


Fig. 2: Control structure of the M3C (see [4])

. For the system voltages

$$\mathbf{v}_X = \sqrt{2} \cdot V_X \cdot \begin{bmatrix} \cos(\theta_X) \\ \cos(\theta_X - \frac{2\pi}{3}) \\ \cos(\theta_X - \frac{4\pi}{3}) \end{bmatrix} \quad \text{and} \quad \mathbf{v}_Y = \sqrt{2} \cdot V_Y \cdot \begin{bmatrix} \cos(\theta_Y + \psi) \\ \cos(\theta_Y - \frac{2\pi}{3} + \psi) \\ \cos(\theta_Y - \frac{4\pi}{3} + \psi) \end{bmatrix} \quad (7)$$

symmetrical waveforms are also assumed. The branch powers $\mathbf{p}_b = \mathbf{i}_b \odot \mathbf{v}_b$ are then obtained by element-wise multiplication of branch currents and branch voltages. In the following, it should additionally be noted that the branch energies \mathbf{e}_b are calculated by integrating the branch powers. This means that the frequencies of the harmonic power components appear in the denominator of the corresponding branch energy components. The following familiar operation modes with different definitions of the circulating currents \mathbf{i}_{cir} are used for comparison purposes in this elaboration:

- Instantaneous Power Mode (IPM) [6]:

$$\mathbf{i}_{cir} = -\frac{1}{4P^*} \cdot \begin{bmatrix} (v_{Y1} \cdot i_{Y1} - v_{Y2} \cdot i_{Y2}) \cdot (i_{X1} - i_{X2}) \\ (v_{Y1} \cdot i_{Y1} - v_{Y2} \cdot i_{Y2}) \cdot (i_{X2} - i_{X3}) \\ (v_{Y2} \cdot i_{Y2} - v_{Y3} \cdot i_{Y3}) \cdot (i_{X1} - i_{X2}) \\ (v_{Y2} \cdot i_{Y2} - v_{Y3} \cdot i_{Y3}) \cdot (i_{X2} - i_{X3}) \end{bmatrix} \quad (8)$$

- Control III (Ctr3) [7]:

$$\mathbf{i}_{cir} = -\frac{1}{4P^*} \cdot \begin{bmatrix} \frac{3}{8} \cdot i_{aa} - \frac{\sqrt{3}}{8} \cdot i_{ab} - \frac{\sqrt{3}}{8} \cdot i_{ba} + \frac{1}{8} \cdot i_{bb} \\ \frac{\sqrt{3}}{4} \cdot i_{ab} - \frac{1}{4} \cdot i_{bb} \\ \frac{\sqrt{3}}{4} \cdot i_{ba} - \frac{1}{4} \cdot i_{bb} \\ \frac{1}{2} \cdot i_{bb} \end{bmatrix} \quad \text{with} \quad \begin{bmatrix} i_{aa} \\ i_{ab} \\ i_{ba} \\ i_{bb} \end{bmatrix} = \frac{I_Y \cdot V_Y}{\sqrt{2} \cdot V_X} \cdot \begin{bmatrix} \cos(\theta_3) \\ \sin(\theta_3) \\ -\sin(\theta_3) \\ \cos(\theta_3) \end{bmatrix} \quad (9)$$

$$\text{with } \theta_3 = \theta_X + 2 \cdot (\theta_Y + \psi) - \phi_Y.$$

It should be noted that the conventions of the circulating currents are different in the references and for the purposes of this paper have been transformed into the configuration shown in Fig. 1 (b). In addition, the star-point voltage of the operation modes considered is assumed to be zero, $v_{st} = 0$. For each operation mode, Table I shows the frequency components resulting from the analytical model for the circulating currents, branch currents and branch energies.

Table I: Frequency components of the operation modes

	NM	IPM	Ctr3
\mathbf{i}_{cir}	-	$f_X + 2f_Y, f_X - 2f_Y$	$f_X + 2f_Y$
\mathbf{i}_b	f_X, f_Y	$f_X, f_Y, f_X + 2f_Y, f_X - 2f_Y$	$f_X, f_Y, f_X + 2f_Y$
\mathbf{e}_b	$2f_X, 2f_Y, f_X \pm f_Y$	$2f_X, f_X \pm 3f_Y, f_X \pm f_Y, 2f_X \pm 2f_Y$	$2f_X, f_X + f_Y, 2f_X + 2f_Y, f_X + 3f_Y$

Table II: Parameters of the M3C analytical model ($k = 100$, only first row is used) and the MMC test bench prototype ($k = 1$)

System voltages	Power setpoint	Modules per branch	System frequencies	Reference values
$V_{X,s}; V_{Y,s}$	P_o^*	n_{mpb}	$f_X; f_Y$	$I_{b,ref}; \Delta e_{b,ref}$
$k \cdot \frac{80}{\sqrt{2}} \text{ V}$	$k^2 \cdot 1800 \text{ W}$	exp.: 6; analyt.: 16	50Hz, 10Hz	$k \cdot \frac{15}{\sqrt{2}} \text{ A}; k^2 \cdot 7 \text{ J}$
Branch inductance	Module capacitance	System X filter	System Y impedance	System Y filter
L_b	$C_{mod,max}$	$L_{X,f}$	$L_Y; R_Y$	$L_{X,f}$
$350 \mu\text{H}$	exp.: 324 μF ; analyt.: 992 μF	1.7mH	$165 \mu\text{H}; 5 \text{ m}\Omega$	3.13mH

If it is assumed that f_X remains constant at 50 Hz and f_Y varies from 0 to 50 Hz, the branch energy components of the Normal Mode (NM), oscillating with $2f_Y$, become very large at frequencies close to zero. For this reason, different frequency components of the circulating currents are injected in the IPM and Ctr3, so that the frequency components of $2f_Y$ are eliminated in the branch energies. To investigate this for several operating points, the branch energy variation $\Delta e_b = \max(e_{bij}) - \min(e_{bij})$ and the RMS branch current $I_b = I_{bij}$ are shown in Fig. 3 (a) for the converter parameters ($k = 100$) of Table II, depending on the variable frequency f_Y . In this case, the analytical model is to represent a medium-voltage converter with 3300 V IGBT modules (Infineon - FZ1400R33HE4) and module capacitors with a capacitance of $C_{mod} = C_{mod,max} = 992 \mu\text{F}$. Based on the components used, the limit values of the module voltages are set to $v_{mod,max} = 3150 \text{ V}$ and $v_{mod,min} = 1050 \text{ V}$. It becomes obvious in the plot of Δe_b that the NM, in contrast to the IPM and Ctr3, is not suitable for low frequencies of f_Y . However, the IPM and Ctr3 have the disadvantage that the RMS value of the branch currents, as an indicator of the branch losses, is much larger due to the injection of the circulating currents. For this reason, it will be investigated in the following section which circulating currents have to be injected to achieve the best trade-off between branch energy variations and branch losses.

Novel Operation Mode with a Dimensioning Optimisation Algorithm

To describe the trade-off between the branch current and the branch energy variation, the following function ξ_{opt} is introduced:

$$\xi_{opt}(\kappa, \mathbf{f}_\kappa, f_Y) = \frac{1}{2} \cdot \left(w_{eb} \cdot \frac{\Delta e_b(\kappa, \mathbf{f}_\kappa, f_Y)}{\Delta e_{b,ref}} + w_{ib} \cdot \frac{I_b(\kappa, \mathbf{f}_\kappa, f_Y)}{I_{b,ref}} \right). \quad (10)$$

with $\kappa = [\kappa_1 \ \kappa_2 \ \dots]^T$ and $\mathbf{f}_\kappa = [f_{\kappa 1} \ f_{\kappa 2} \ \dots]^T$. The dimension of the vectors depends on how many frequency components are used for the circulating currents. In the following, it is assumed that the circulating currents have two frequency components, like for Ctr3 and IPM, so that the calculation of the dimensioning algorithm with the analytical model does not require excessively long time. Both the branch energy variation $\Delta e_b(\kappa, \mathbf{f}_\kappa, f_Y)$ and the RMS value $I_b(\kappa, \mathbf{f}_\kappa, f_Y)$ in Equation (10) are dependent on the circulating currents, which are defined as follows

$$\mathbf{i}_{circ} = \sqrt{2} \cdot I_{circ} \cdot \begin{bmatrix} \kappa_1 \cdot \cos(\theta_{\kappa 1} + \varphi_{\kappa 1,1}) + \kappa_2 \cdot \cos(\theta_{\kappa 2} + \varphi_{\kappa 2,1}) \\ \kappa_1 \cdot \cos(\theta_{\kappa 1} + \varphi_{\kappa 1,2}) + \kappa_2 \cdot \cos(\theta_{\kappa 2} + \varphi_{\kappa 2,2}) \\ \kappa_1 \cdot \cos(\theta_{\kappa 1} + \varphi_{\kappa 1,3}) + \kappa_2 \cdot \cos(\theta_{\kappa 2} + \varphi_{\kappa 2,3}) \\ \kappa_1 \cdot \cos(\theta_{\kappa 1} + \varphi_{\kappa 1,4}) + \kappa_2 \cdot \cos(\theta_{\kappa 2} + \varphi_{\kappa 2,4}) \end{bmatrix} \quad (11)$$

with $\varphi_{\kappa 1} = [\varphi_{\kappa 1,1} \ \varphi_{\kappa 1,2} \ \varphi_{\kappa 1,3} \ \varphi_{\kappa 1,4}]^T$ and $\varphi_{\kappa 2} = [\varphi_{\kappa 2,1} \ \varphi_{\kappa 2,2} \ \varphi_{\kappa 2,3} \ \varphi_{\kappa 2,4}]^T$

with $\theta_{\kappa 1} = 2\pi \cdot f_{\kappa 1} \cdot t$ and $\theta_{\kappa 2} = 2\pi \cdot f_{\kappa 2} \cdot t$. Due to the fact that the branch energies and the branch currents have different units and scalings, they are normalised with the reference values $\Delta e_{b,ref}$ and $I_{b,ref}$, which represent the specified maximum values of the converter components. The maximum value $I_{b,ref} = I_{b,max}$ of the RMS branch current is determined with the help of the data sheet of the semiconductor used in the modules (mostly IGBTs) and should be below the defined maximum value of the continuous DC collector current. In order to limit the range of the circulating current RMS value, it is assumed that

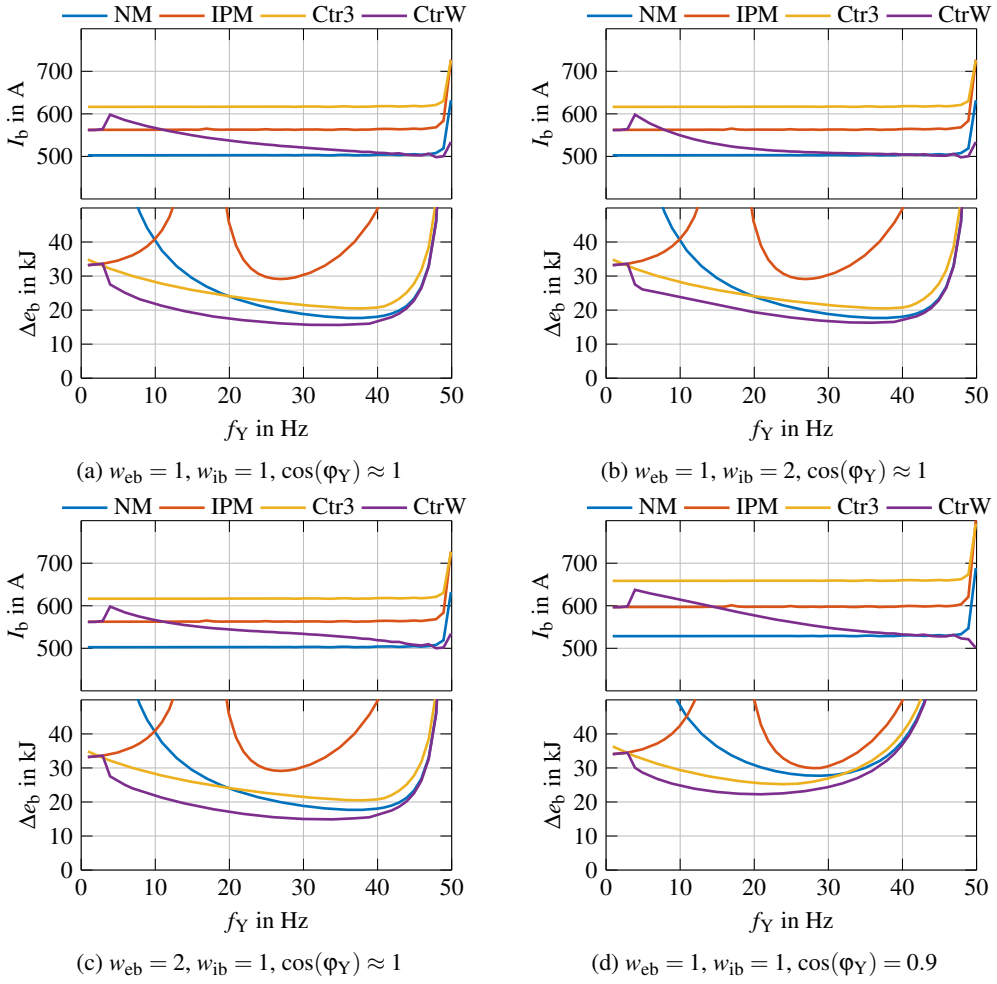


Fig. 3: Comparision of the operation modes regarding the branch energy variation and the branch current RMS value at different frequencies of f_Y with different weighting factors (a) - (c) and a different phase angle φ_Y (d) with $\psi = \varphi_X = 0$.

$\kappa_1 \cdot I_{\text{circ}_K}$ or $\kappa_2 \cdot I_{\text{circ}_K}$ does not exceed the reference value of the branch current $I_{b,\text{ref}}$. For this reason, I_{circ_K} is chosen equal to the reference value of the branch currents $I_{\text{circ}_K} = I_{b,\text{ref}}$ and κ_1 and κ_2 vary from 0 to 1. The reference value of the branch energy variation

$$\Delta e_{b,\text{ref}} = \Delta e_{b,\text{max}} = \frac{1}{2} \cdot C_{\text{mod},\text{max}} \cdot n_{\text{mod}} \cdot (v_{\text{mod},\text{max}}^2 - v_{\text{mod},\text{min}}^2) \quad (12)$$

is calculated using the maximum desired module capacitance $C_{\text{mod},\text{max}}$, the number of modules per branch n_{mod} , the maximum $v_{\text{mod},\text{max}}$ and minimum value $v_{\text{mod},\text{min}}$ of the module voltages. In addition, the weighting factors w_{eb} and w_{ib} are introduced so that some variability in the trade-off function ξ_{opt} is still possible. For each operating point of f_Y , the minimum is calculated from the weighting function for circulating currents with variable frequencies and amplitudes: $\min(\xi_{\text{opt}}(\kappa, \mathbf{f}_\kappa, f_Y)) \rightarrow \kappa_{\text{opt}}, \mathbf{f}_{\kappa,\text{opt}}$. For each operating point, an optimal set of parameters $(\kappa_{\text{opt}}, \mathbf{f}_{\kappa,\text{opt}})|_{f_Y}$ is then obtained for the circulating currents.

As an example, in Fig. 4 (a), the weighting function ξ_{opt} is shown for an operating point of $f_Y = 10\text{Hz}$ when only one parameter κ_1 is active. In the zoomed-in plots shown alongside, it becomes visible that especially at the frequencies $f_{\kappa_1} = 30\text{Hz}$, $f_{\kappa_1} = 70\text{Hz}$, $f_{\kappa_1} = 90\text{Hz}$ the weighting function is comparatively small. The minimum of the weighting function is at the operating point for the operating point of $f_Y = 10\text{Hz}$ is located at the parameter set $(f_{\kappa_1,\text{opt}} = 70\text{Hz}, \kappa_{1,\text{opt}} = 0.6)|_{10\text{Hz}}$. In Fig. 4 (d), the calculated optimal parameters shown for several operating points. With the dotted plot of $\kappa_{1,\text{opt}}$ and $\kappa_{2,\text{opt}}$ the calculated optimal parameters at which ξ_{opt} reaches a minimum for different operating points are shown. To avoid having to examine an infinite number of operating points, the circulating current frequencies f_{κ_1}

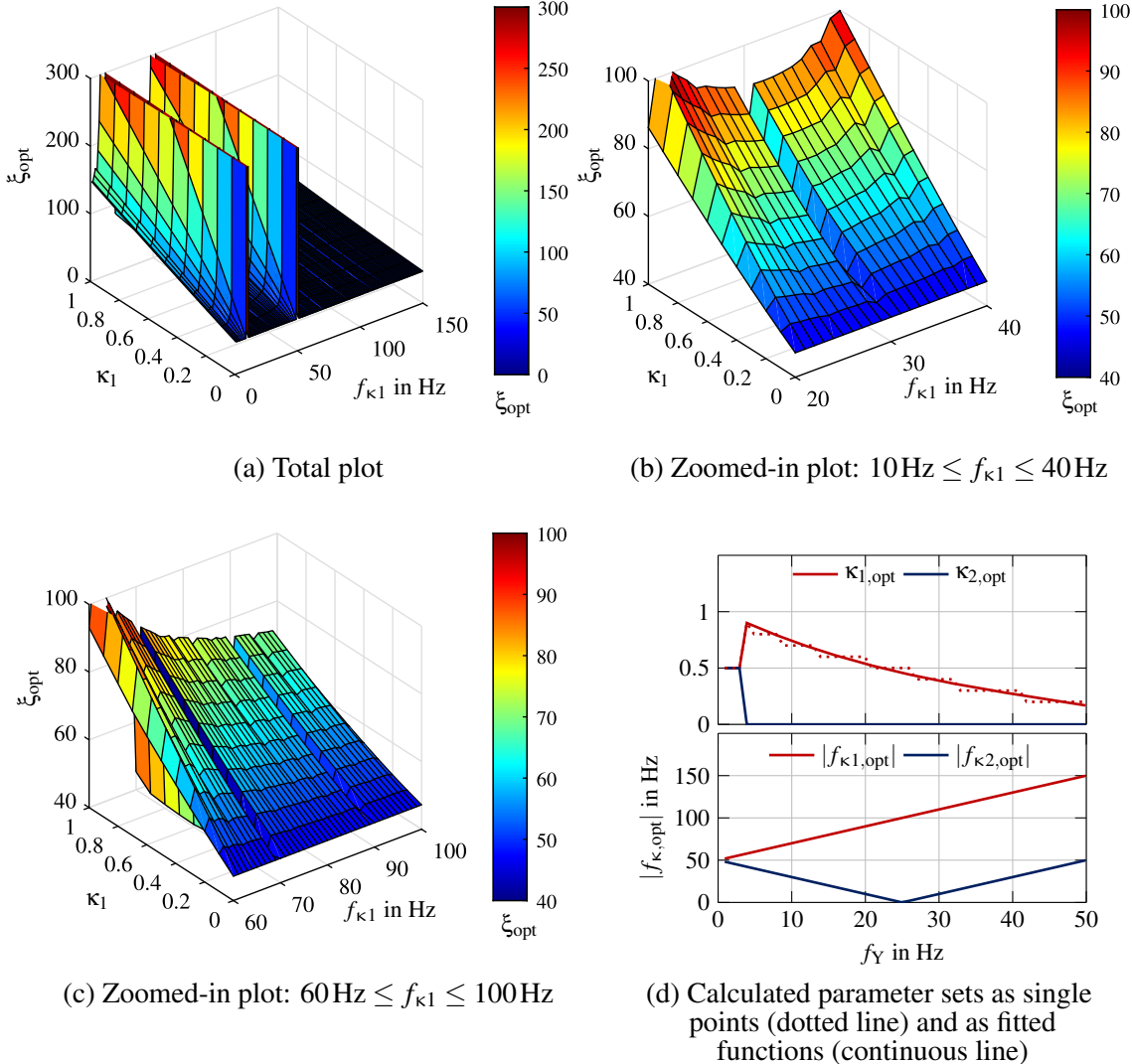


Fig. 4: (a) - (c): Weighting function ξ_{opt} surface plots at $f_Y = 10\text{Hz}$ depending on κ and \mathbf{f}_κ and (d) the optimal parameter sets for $f_Y = 1\text{Hz}$ to 50Hz . Parameters: $\psi = \varphi_X = \varphi_Y = 0$, $w_{\text{ib}} = w_{\text{eb}} = 1$. Minimum of ξ_{opt} for $f_Y = 10\text{Hz}$: $(f_{\kappa 1,\text{opt}} = 70\text{Hz}, f_{\kappa 2,\text{opt}} = 30\text{Hz}, \kappa_{1,\text{opt}} = 0.6, \kappa_{2,\text{opt}} = 0.0)|_{10\text{Hz}}$.

and $f_{\kappa 2}$ are analysed in the interval of $1\text{Hz} : 1\text{Hz} : 3 \cdot f_X$ and amplitude factors κ_1 and κ_2 in the interval of $0 : 0.1 : 1$ for each operating point $1\text{Hz} : 1\text{Hz} : 50\text{Hz}$ of the system frequency f_Y . To ensure that the points in between are also taken into account, the points are approximated by third-degree polynomials

$$\kappa_{1,\text{fit}}(f_Y) = q_{13} \cdot f_Y^3 + q_{12} \cdot f_Y^2 + q_{11} \cdot f_Y + q_{10} \quad \text{with } \mathbf{q}_1 = [q_{10} \quad q_{11} \quad q_{12} \quad q_{13}]^T, \quad (13)$$

$$\kappa_{2,\text{fit}}(f_Y) = q_{23} \cdot f_Y^3 + q_{22} \cdot f_Y^2 + q_{21} \cdot f_Y + q_{20} \quad \text{with } \mathbf{q}_2 = [q_{20} \quad q_{21} \quad q_{22} \quad q_{23}]^T. \quad (14)$$

In the designed optimisation algorithm, the `polyfit()` function of MATLAB is used to execute this regression and provide the coefficients \mathbf{q}_1 and \mathbf{q}_2 . Instead of transferring an infinite number of points as a look-up table into the model, the fitted functions $\kappa_{1,\text{fit}}$ and $\kappa_{2,\text{fit}}$ are included in the calculation of the circulating currents in Equation (11). Furthermore, the minima of ξ_{opt} is always at $f_{\kappa 1} = f_X + 2f_Y$ and $f_{\kappa 2} = f_X - 2f_Y$ like shown in Fig. 4 (d). Although κ_2 and $f_{\kappa 2}$ are only required at low frequencies. With this conclusions, the computational time of the optimisation algorithm can be reduced, as $f_{\kappa 1}$ and $f_{\kappa 2}$ can be determined by the system frequencies. Additionally, the phase shifts $\varphi_{\kappa 1}$ and $\varphi_{\kappa 2}$ are also a solution of the optimisation algorithm without dependence on the frequency f_Y :

- Case 1 with $\varphi_{\kappa 1} = [-\varphi_X - \varphi_Y \quad -\frac{2\pi}{3} - \varphi_X - \varphi_Y \quad -\frac{4\pi}{3} - \varphi_X - \varphi_Y \quad -\varphi_X - \varphi_Y]^T$ and $\varphi_{\kappa 2} = [\frac{\pi}{3} - \varphi_X + \varphi_Y \quad -\frac{\pi}{3} - \varphi_X + \varphi_Y \quad -\frac{\pi}{3} - \varphi_X + \varphi_Y \quad \pi - \varphi_X + \varphi_Y]^T$ if κ_1 and κ_2 are active,
- Case 2 with $\varphi_{\kappa 1} = [-\varphi_Y \quad -\frac{2\pi}{3} - \varphi_Y \quad -\frac{4\pi}{3} - \varphi_Y \quad -\varphi_Y]^T$ if only κ_1 is active.

By including the adjusted circulating currents \mathbf{i}_{circ} in the analytical equations from the previous section, the branch energy variation and RMS branch current of the novel operation mode with the weighting function, named Control W (CtrW), can be displayed for each operating point. In this publication, only the influences of the circulating currents as degrees of freedom are investigated and the star-point voltage ($v_{st} = 0$) is not considered, which as in reference [9] are used to compensate the significant high branch energy variation for $f_Y \approx f_X$. Fig. 3 shows in purple the plot of CtrW for the listed (converter) parameters of Table II. It can be seen that both the branch energy variation and the branch current can be reduced in contrast to the Ctr3 and thus a better trade-off can be found for frequencies below 25 Hz. For frequencies above 25 Hz, the CtrW approximates the NM, since the additional injection of circulating currents is no longer necessary. The analytical results show that the CtrW has advantages especially in the lower frequency ranges of f_Y , because a suitable trade-off between branch energy variation and branch currents can be found.

Validation of the Novel Operation Mode

For the validation of the novel operation modes, the control structure from Fig. 2 is used. The additional setpoints of the circulating currents are equal to the analytically calculated circulating currents from the last sections: $\mathbf{i}_{\text{cir,add}} = \mathbf{i}_{\text{circ}}$ of (11). This means that in steady state, the setpoints of the circulating currents $\mathbf{i}_{\text{cir}}^*$ correspond to the analytically calculated values $\mathbf{i}_{\text{cir,add}}$. In order to better compare the experimental results with the medium-voltage analytical model, both currents and voltages were scaled down by a factor of $k = 100$ for the measurements, so that the same parameter functions $\kappa_{1,\text{fit}}(f_Y)$ and $\kappa_{2,\text{fit}}(f_Y)$ of the CtrW can be implemented in the control system of the test bench for various operating points of f_Y (Table II). In Fig. 5 (a) the low-voltage test bench of the M3C is shown and in Fig. 5 (b) the implementation of the control structure is visualised. The voltage of system X is provided by the 400 V/50 Hz grid and transformers. On the other hand, system Y is supplied via a microgrid from the company Triphase, so that a variable frequency f_Y is possible. In the M3C, 120 V MOSFETs (Infineon - IPB036N12N3-G) are integrated in the 54 modules (nine branches, each six installed modules). The limitation of the module voltage is set to $v_{\text{mod,max}} = 90\text{V}$, $v_{\text{mod,min}} = 30\text{V}$ and the maximum required module capacitance to $C_{\text{mod,max}} = 324\mu\text{F}$. Here, the actual installed module capacitance is not taken into account, as this was designed for relatively large branch energy variation.

To verify that the control works in principle, Fig. 6 shows the active switching ($t = 150\text{ms}$) for the operating point $f_Y = 10\text{Hz}$ from NM to CtrW. In addition to the system voltages \mathbf{v}_X , \mathbf{v}_Y measured behind the filter inductances ($L_{X,f}$, $L_{Y,f}$), the branch current i_{b11} and the branch energy control deviation \tilde{e}_{b11} (defined in Fig. 2) are also displayed. It can be seen that the branch energy control is working and that, as shown in Fig. 3 (a) at $f_Y = 10\text{Hz}$, the branch energy variation of the CtrW becomes smaller and the branch current larger compared to the NM. Moreover in Fig. 7, the measured circulating currents are shown. From time $t = 150\text{ms}$ onwards, additional circulating currents are injected by the CtrW, in order to reduce the branch energy variations. This results in increased branch currents and thus increased branch losses in contrast to the NM.

Finally, the analytical model is to be validated using the experimental steady state waveforms and compared with the analytical results. In Fig. 8 the branch currents and branch energies of the analytical model and of the test bench are shown. The parameter Δt_{steady} represents the time until the steady state of the measured values are reached. The phase shift between the systems ψ , which is not equal to zero for the measurements, is determined with the help of the time shift of both angles θ_X and θ_Y . In order to better compare the waveforms in Fig. 8, this resulting phase angle ψ was also included in the calculations of the analytical waveforms. Except for the switching harmonics and the parasitic influences on the test bench, the analytical and experimental waveforms match in amplitude and frequency components. In summary, the experimental results show that the dimensioning algorithm based on the analytical model also works for the test bench.

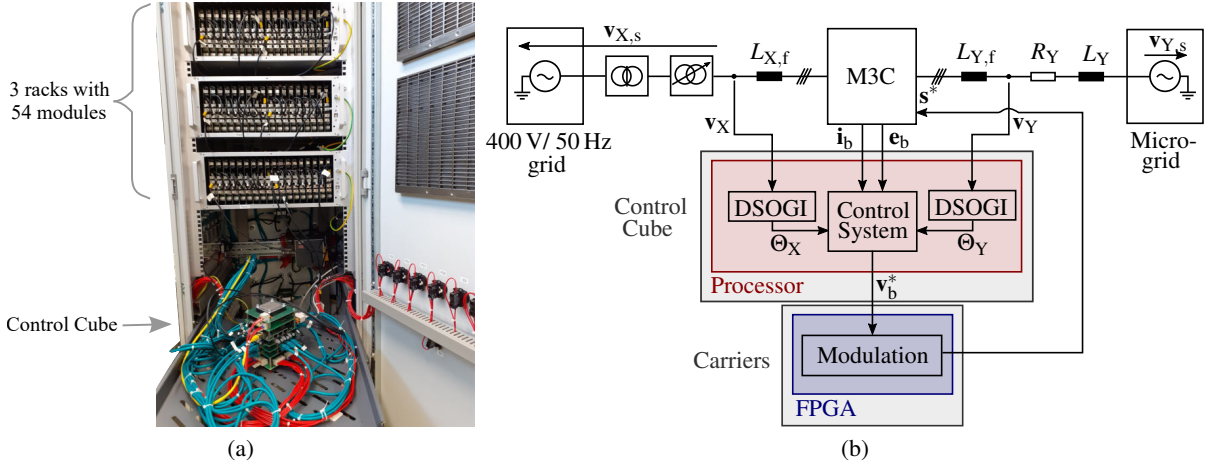


Fig. 5: (a) Low-voltage test bench of the M3C and (b) test bench set-up schematic.

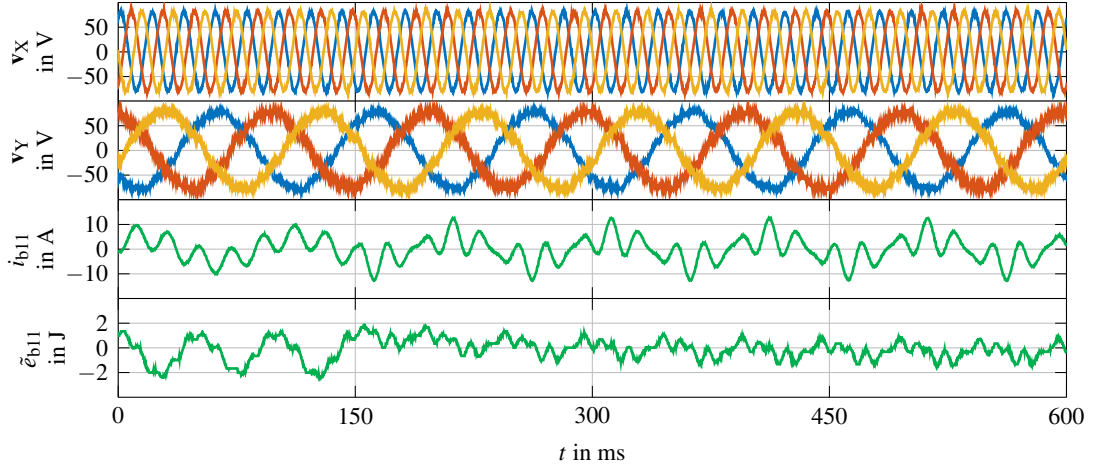


Fig. 6: Measured waveforms of the system voltages, branch current and branch energy during an active switchover from NM to CtrW at $t = 150\text{ms}$ for $f_Y = 10\text{Hz}$. Parameters: $\varphi_X = \varphi_Y = 0$, $w_{ib} = w_{eb} = 1$. Minimum of ξ_{opt} for $f_Y = 10\text{Hz}$: $(f_{k1,\text{opt}} = 70\text{Hz}, f_{k2,\text{opt}} = 30\text{Hz}, \kappa_{1,\text{opt}} = 0.6, \kappa_{2,\text{opt}} = 0.0)|_{10\text{Hz}}$.

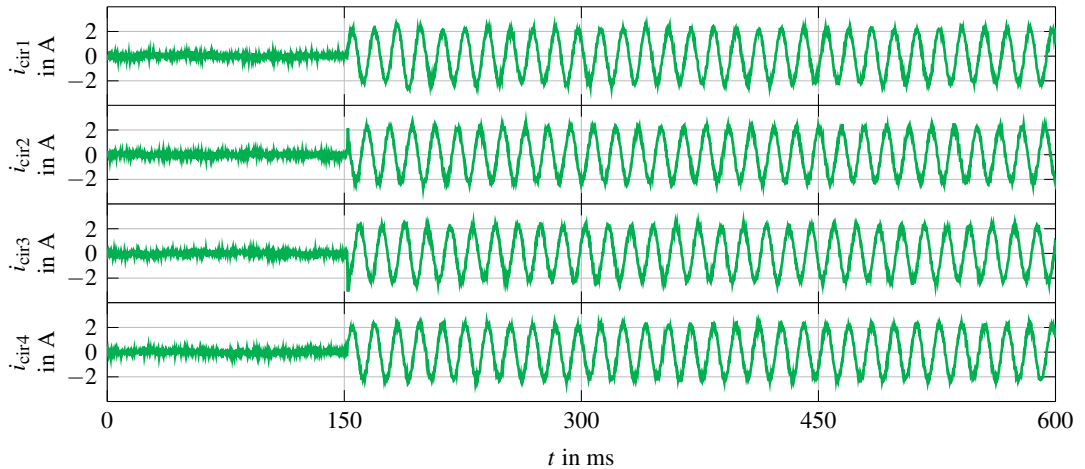


Fig. 7: Measured waveforms of the circulating currents during an active switchover from NM to CtrW at $t = 150\text{ms}$ for $f_Y = 10\text{Hz}$. Parameters: $\varphi_X = \varphi_Y = 0$, $w_{ib} = w_{eb} = 1$. Minimum of ξ_{opt} for $f_Y = 10\text{Hz}$: $(f_{k1,\text{opt}} = 70\text{Hz}, f_{k2,\text{opt}} = 30\text{Hz}, \kappa_{1,\text{opt}} = 0.6, \kappa_{2,\text{opt}} = 0.0)|_{10\text{Hz}}$.

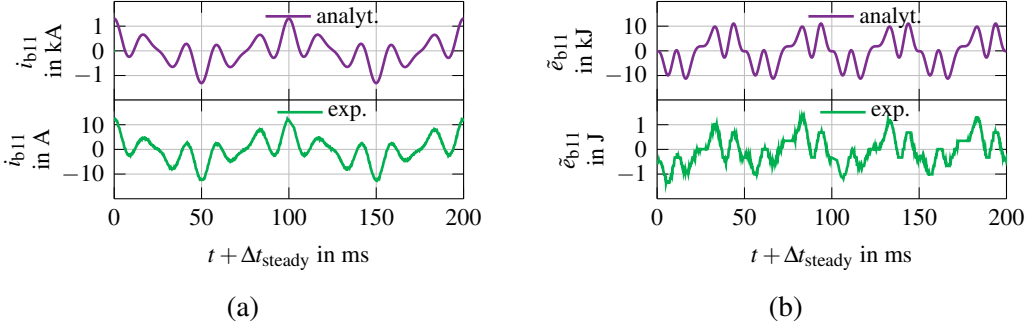


Fig. 8: Comparison of the calculated (analyt.) and measured waveforms (exp.) of (a) the branch currents and (b) branch energies of the CtrW at $f_Y = 10$ Hz. Parameters: $\varphi_X = \varphi_Y = 0$, $w_{ib} = w_{eb} = 1$. Minimum of ξ_{opt} for $f_Y = 10$ Hz: $(f_{k1,\text{opt}} = 70$ Hz, $f_{k2,\text{opt}} = 30$ Hz, $\kappa_{1,\text{opt}} = 0.6$, $\kappa_{2,\text{opt}} = 0.0)|_{10\text{Hz}}$.

Conclusion

Both the results of the analytical model and the experimental results have shown that an optimal weighting between installed module capacitances and losses in the branch can be found in contrast to the other operation modes considered, especially at lower frequencies, by applying the new operation mode (Control W). This is particularly interesting in machine applications or LF-HVAC where the components such as module capacitances and IGBT modules are predefined and the branch losses are to be reduced at lower frequencies. Therefore, it is necessary to have a more detailed knowledge of the converter's parameters and limitations in order to achieve the best optimisation result.

References

- [1] M. Glinka and R. Marquardt, “A New AC/AC-Multilevel Converter Family Applied to a Single-Phase Converter,” *The Fifth International Conference on Power Electronics and Drive Systems, 2003*, vol. 1, pp. 16–23, 2003.
- [2] F. Kammerer et. al, “Operating Performance of the Modular Multilevel Matrix Converter in Drive Applications,” *PCIM Europe 2015; International Exhibition and Conference for Power Electronics, Intelligent Motion, Renewable Energy and Energy Management; Proceedings of*, no. May, pp. 19–21, 2015.
- [3] Y. Tang et. al, “Offshore low frequency AC transmission with back-to-back modular multilevel converter (MMC),” *IET Seminar Digest*, vol. 2015, no. CP654, pp. 1–8, 2015.
- [4] D. Karwatzki et. al, “Generalized Control Approach for a Class of Modular Multilevel Converter Topologies,” *IEEE Transactions on Power Electronics*, vol. 33, no. 4, pp. 2888–2900, 2018.
- [5] F. Kammerer et. al, “A novel cascaded vector control scheme for the Modular Multilevel Matrix Converter,” *IECON Proceedings (Industrial Electronics Conference)*, pp. 1097–1102, 2011.
- [6] A. J. Korn et. al, “Direct Modular Multi-Level Converter for Gearless Low-Speed Drives,” *Proceedings of the 2011 14th European Conference on Power Electronics and Applications, EPE 2011*, 2011.
- [7] W. Kawamura et. al, “Control and Experiment of a Modular Multilevel Cascade Converter Based on Triple-Star Bridge Cells,” *IEEE Transactions on Industry Applications*, vol. 50, no. 5, pp. 3536–3548, 2014.
- [8] F. Kammerer et. al, “Energy Balancing of the Modular Multilevel Matrix Converter based on a New Transformed Arm Power Analysis,” *2014 16th European Conference on Power Electronics and Applications, EPE-ECCE Europe 2014*, pp. 1–10, 2014.
- [9] W. Kawamura et. al, “Experimental Verification of an Electrical Drive Fed by a Modular Multilevel TSBC Converter When the Motor Frequency Gets Closer or Equal to the Supply Frequency,” *IEEE Transactions on Industry Applications*, vol. 53, no. 3, 2017.
- [10] S. P. Engel et. al, “Control of the modular multi-level converter for minimized cell capacitance,” *Proceedings of the 2011 14th European Conference on Power Electronics and Applications, EPE 2011*, pp. 1–10, 2011.
- [11] B. Fan et. al, “An Optimal Full Frequency Control Strategy for the Modular Multilevel Matrix Converter Based on Predictive Control,” *IEEE Transactions on Power Electronics*, vol. 33, no. 8, pp. 6608–6621, 2018.